BCC-FCC interfacial effects on plasticity and strengthening mechanisms in high entropy alloys

Basu, Indranil; Ocelík, Václav; De Hosson, Jeff Th M.

Published in:
Acta Materialia

DOI:
10.1016/j.actamat.2018.07.031

Publication date:
2018

BCC-FCC interfacial effects on plasticity and strengthening mechanisms in high entropy alloys

Indranil Basu, Václav Ocelík, Jeff Th.M De Hosson*

Department of Applied Physics, Zernike Institute for Advanced Materials and Materials innovation institute, University of Groningen, 9747AG Groningen, The Netherlands

Abstract

$Al_{0.7}$CoCrFeNi high entropy alloy (HEA) with a microstructure comprising strain free face-centered cubic (FCC) grains and strongly deformed sub-structured body centered cubic (BCC) grains was subjected to correlative nanoindentation testing, orientation imaging microscopy and local residual stress analysis. Depending on the geometry of BCC-FCC interface, certain boundaries indicated appearance of additional yield excursions apart from the typically observed elastic to plastic displacement burst. The role of interfacial strengthening mechanisms is quantified for small scale deformation across BCC-FCC interphase boundaries. An overall interfacial strengthening of the order of $4\,GPa$ was estimated for BCC-FCC interfaces in HEAs. The influence of image forces due to the presence of a BCC-FCC interface is quantified and correlated to the observed local stress and hardness gradients in both the BCC and FCC grains.

Keywords: nanoindentation; electron back scatter diffraction; residual stress; dislocations; interphase boundary

* Corresponding author. E-mail address: j.t.m.de.hosson@rug.nl (jeff th m dehosson).

1. Introduction

Recent studies on microstructural development in multiphase HEAs [1–5] have successfully showed that significant enhancement in structural properties over conventional steels is achievable, whereby the much debated strength-ductility trade-off effect can be surpassed in these alloys [6–9]. For instance, one of the relatively well researched HEAs, $Al_xCoCrFeNi$, is known to transition from solid solution FCC to mixture of FCC and BCC phases with increasing Al content [10]. Theoretically the multiphase $Al_xCoCrFeNi$ alloy can possess the benefits of both a ductile FCC phase along with the strength increment imparted by the BCC constituent phases. Yet for designing multiphase HEAs with enhanced mechanical properties, it is essential to surmise the mechanistic contribution of interfaces present between compositionally or crystallographically dissimilar phases to the local deformation response and associated strengthening behavior.

Compared to classical grain boundaries, heterophase interfaces seem to require much higher stresses for strain transmission. In case of grain boundaries in single phase materials, extensive experimental work [11–13] has been devoted to identify the primary interface characteristics that govern strain transfer. These analyses predict the feasibility of slip transmission to be dependent upon the geometrical alignment of the active slip systems across the interface and the minimization of dislocation energy at the boundary. Mathematically, this can be quantified by the slip transfer parameter m', expressed as[11,12],

$$m' = (\boldsymbol{n_1} \cdot \boldsymbol{n_2}).(\boldsymbol{b_1} \cdot \boldsymbol{b_2}) \qquad (1)$$

where $\boldsymbol{n_1}$ and $\boldsymbol{n_2}$ are the normalized intersection lines common to the slip planes and the boundary plane, and $\boldsymbol{b_1}$ and $\boldsymbol{b_2}$ are the normalized slip directions in the pile-up and emission grains. The first expression in parentheses on the right hand side of Eqn. 1 correlates to the

alignment of the incoming and outgoing slip planes active in the incident and emission grains. Maximization of this value directly corresponds to the minimization of the angle between the neighboring slip planes. Similarly the trailing expression on the right hand side determines the geometric alignment of the incoming and outgoing slip directions, maximization of which correlates to minimization of magnitude of the residual burgers vector left in the interface. In total, maximization of m' is associated with lower grain boundary obstacle strength and energetically easier slip transfer across the interface.

However, for assessing strain transfer across interfaces between crystallographically different phases, application of the aforementioned geometrical rules may be inadequate to fully comprehend the experimentally observed behavior. This primarily stems from the additional contribution of interface-dependent strengthening mechanisms present in heterophase materials (such as BCC-FCC interfaces) that significantly alter dislocation-interface interactions and internal stress configurations. In the classical approximation, the blocking strength of bimetallic interfaces, apart from the geometrical feasibility of slip transmission, is dependent upon the superposition of primarily three strengthening effects viz. i) elastic moduli mismatch (‘image’ or ‘Koehler’ stresses) [14,15], ii) lattice parameter mismatch (‘misfit’ stresses) [16] and iii) stacking fault or chemical mismatch effect [17]. Slip transmission in such case occurs when the resolved shear stress in the emission grain exceeds the interfacial strengthening stress.

It is well established that the contribution of interfacial plasticity becomes more and more significant as the length scales of plastic deformation reduce. Wang and Misra [18] suggested that the nature of interaction of interfaces with lattice dislocations strongly depends on the interfacial shear strength. It was found that non-coherent BCC-FCC interfaces, described by a Kurdjumov-Sachs type orientation relationship, display low interfacial shear strengths. Such interfaces contribute to local deformation by absorbing

incoming lattice dislocations that subsequently spread their dislocation cores within the interface. The width of spread core increases with decreasing interface shear strengths. In order to nucleate slip into the neighboring grain, the dislocation core needs to undergo shrinkage. This is achieved by dissociation of the absorbed dislocation into in-plane and out-of-plane components, wherein the former glide freely along the interface subsequently shearing it and the latter participate in vacancy climb mechanisms resulting in normal displacement of the interphase boundary segment into the emission grain. In another study [19], it was shown that the strength contribution (sum total of the three strengthening mechanisms) from incoherent BCC-FCC interphase boundaries (~ 0.33 – 1.09 GPa) is lower than strength values for interfaces in single phase BCC materials (~ 1.2 GPa) as well as for coherent FCC-FCC interfaces (~ 0.6 – 1.42 MPa) that show large contribution from 'misfit' stresses. The mechanism of interface shear by lattice dislocations as described in ref. [18] was suggested as the key mechanism behind the weakening effect displayed by BCC-FCC interfaces.

The results and discussions presented in the current work highlight the deformation mechanisms near/at BCC-FCC interfaces in HEAs. Insights are drawn on the influence of interfacial strengthening mechanisms and the corresponding influence upon dislocation-phase boundary interactions. Additionally, comparisons are drawn between BCC-FCC interfaces in HEAs vis-à-vis those in conventional alloys. The overall effect is subsequently gauged in terms of interfacial resistance to damage nucleation.

2. Experimental methodology

Multiphase high entropy alloys with nominal composition of $Al_{0.7}CoCrFeNi$ were prepared and subjected to hot forging as described in refs. [5,20]. Scanning electron microscopy (SEM) and electron back scattered diffraction (EBSD) technique were utilized for

characterizing the local microstructure and crystallographically different phases. SEM/EBSD measurements were made using a Tescan Lyra dual beam (FEG-SEM/FIB) scanning electron microscope equipped with an EDAX TSL EBSD system with Hikari Super CCD camera used for acquiring EBSD patterns. An electron beam accelerating voltage of 25kV and current of 20nA was used. A step size of 75 nm and hexagonal type of grid was used for collection of EBSD data. A binning width of *2 x 2* was used for collection of Kikuchi patterns using 640x480 CCD camera resolution. The acquired raw EBSD data was subsequently analyzed using EDAX-TSL OIM™ Analysis 7.3 software and *MTEX* Matlab based toolbox [21]. Noise reduction was performed with a threshold confidence interval of 0.2. The orientation of the phase boundary plane was determined by milling into the region containing the boundary using focused ion beam (FIB) and examining the boundary trace along the milled cross section.

Instrumented nanoindentation measurements were carried out employing an MTS Nano Indenter XP (MTS Nano Instruments, Oak Ridge, TN) with a cube-corner tip (with centerline-to-face angle $\varphi = 35.26°$) using the continuous stiffness measurement (CSM) technique. Load-controlled indentations were made to a maximum depth of 500 nm with a targeted strain rate of $0.05\ s^{-1}$, which corresponds to a maximum loading rate of the order of $0.1\ mN/s$. All nanoindentation tests were performed at ambient temperatures. Values of hardness (*H*) and Young's modulus (*E*) were obtained from the load–displacement data for the indentations using the Oliver–Pharr method [22].

Indentations were performed at different distances from the BCC-FCC interphase. In order to vary the distance to the BCC-FCC interphase boundary with the smallest possible increments, lines of indentations were drawn at angles $\sim 5° - 8°$ to the phase boundary with a spacing of 3 μm between the indents. The chosen spacing ensured no significant effect of any crosstalk interaction on the measured response. Specimens for indentation were

subjected to mechano-chemical polishing for 60 minutes using 0.02 μm colloidal silica to reduce the influence of mechanical grinding induced deformation layer as well as any possible surface oxide effects on the overall hardness response. Post indentation, specimens were mildly etched with 30 v./v. % H_2O_2 to obtain a clear topographical contrast during electron microscopy imaging.

Local stresses near grain boundaries were experimentally determined by a micro-slit milling technique described in [23–25]. The method relies on the measurement of displacements induced due to stress relaxation in the vicinity of the FIB milled slit. In the current work, linear slits, oriented normal to the phase boundary trace, of a fixed width 0.5 μm, depth 2.5 μm, and lengths varying from 20-25 μm were milled across the phase boundaries showing different degrees of pile-up as per local misorientation data. For each slit, multiple SEM images were acquired at high magnifications (field of view of $\sim$10 μm) to ensure high spatial resolution of measured displacement field.

Displacements lateral to the slit were measured using a commercial digital image correlation (DIC) software GOM Correlate v. 2016. In order to obtain statistically sufficient data points, DIC was performed using a facet size of 41 x 41 pixels with a step width of 21 pixels, such that each facet comprised of sufficient contrast features for image correlation. Yttria-stabilized Zirconia (YSZ) nano-particles were used for surface decoration to obtain optimum image contrast for high accuracy DIC analysis. The stress values in the direction transverse to the slit were subsequently determined by analytical fitting of the measured displacements. A multiple fitting approach to account for spatially heterogeneous stress profiles was adopted. For more details, the reader is referred to [23,24].

Since different materials exhibit differential rates of milling, exact determination of the milled slit depth is necessary for accurate residual stress estimation. This is achieved by site

specific electron beam deposition (EBD) and FIB milling as illustrated in Fig. 1. A part of the slit is filled with Pt from precursor gas using EBD technique (c.f. see inset in Fig. 1). Subsequently the deposited slit is locally milled using FIB down to a depth of 5 μm such that the bottom of the milled slit is visible (c.f. Fig. 1). The stage was subsequently tilted to $\theta_{tilt} = 50^{\circ}$ and SEM imaging was performed to capture the complete slit depth profile. Imaging is performed with tilt compensation in order to obtain the actual milling depth (h_{actual}) of 2.36 μm.

3. Results

Local stress measurement and nanoindentation tests were performed across two different BCC-FCC interphase boundaries, enclosed by *Area 1* and *Area 2* respectively (c.f. Fig.2a). The interphase boundaries enclosed in each area are differentiated on the basis of their geometrical feasibility to allow slip transmission, as per Eqn. 1.

Blocked dislocation arrays

Fig.2b provides the local misorientation distribution in the form of the kernel average misorientation (KAM) and local average misorientation (LAM) maps corresponding to the region marked as *Area 1*. BCC-FCC interphase boundaries are highlighted in white and the grain boundaries are shown in black, described by threshold misorientation of 3°. The location of the indents and milled slit (depicted by the line AB) is schematically shown in Fig.2b. Indents were made in the BCC grain at increasing distance from the BCC-FCC phase boundary, with distances varying from 40nm to 3µm. A threshold misorientation angle of 2° and nearest neighbor value of 2 was used. The KAM and LAM maps indicate significant plastic strain accumulation in the BCC grain with misorientation gradients close to the phase boundary, indicating dislocation pile-up. On the other hand, the adjacent FCC grain is devoid of any strain localization as indicated by very low local misorientation values. Fig.3a

shows the SEM image of the indents made in the vicinity of BCC-FCC phase boundary. Indents very close to the phase boundary, generated dislocation strain fields that could penetrate the FCC grain, as shown in the magnified SEM image in Fig.3a. The slip transfer parameter across the interphase boundary was calculated as $m' = 0.0432$, indicating strong geometrical resistance to slip (c.f. Fig.3a). The active slip system in each grain was determined on the basis of maximization of the Schmid factor (SF) value for a given stress tensor. For the FCC phase 12 slip systems described by $(111) < 1\bar{1}0 >$ were considered, whereas for the BCC grain 48 possible slip systems on $(1\bar{1}0)$, $(11\bar{2})$ and $(12\bar{3})$ planes and along $< 111 >$ slip direction were taken into account for SF calculations [26]. A stress tensor corresponding to uniaxial compressive deformation was utilized. The predicted active slip systems correlated well with the experimentally observed slip traces around indents. Fig 3a additionally shows the grain reference orientation deviation (GROD) map of the indented area corroborating the observed strain fields generated by the indents. Dislocation strain fields are effectively blocked by the grain boundary, for indents made at distances beyond 800 nm (c.f. Fig.3a). The investigated phase boundary was also quantified for local residual stress gradients in the vicinity. The diagram on the right side in Fig.3b shows the SEM image of the orientation of the milled slit perpendicular to the phase boundary. The stress values were measured along the transverse direction with respect to the slit length. The image on the left side in Fig.3b gives the orientation of the boundary plane, inclined towards the FCC grain described by inclination angle of ~105° with respect to the plane of milling. This indicates that grain boundary moves away from the indent with increasing penetration depth and no contact with the interface is expected for indents made inside the BCC grain.

Fig.4 displays the hardness vs. depth curves for indentation in BCC grain interior and at varying distances from the phase boundary. The inset image shows the magnified view of the initial hardness variation. Hardness variation over depth in the grain interior shows a

monotonic decrease with increasing indentation depth, which typically arises due to indentation size effects. In case of indents in the vicinity of the boundary, the hardness response can be classified into different regimes. The hardness values initially decline with increasing indentation depth. However at a certain critical depth $'h_{crit}'$ (highlighted by black arrows in the inset image in Fig.4) the hardness profile starts to increase monotonically with increasing displacement, until it abruptly switches into a rapid drop in hardness (shown by blue and green arrows for two different indent locations in Fig.4). This non-monotonic behavior is repeated more than once (see zones *I* and *II* in Fig. 4 corresponding to indentation at 40nm from phase boundary), with the fluctuations dampening severely beyond zone II and the hardness values reaching a steady state. The observed fluctuations in the hardness values correlate well with the observed displacement bursts seen in load-displacement data. The magnitude of the h_{crit} seems to proportionally increase with the distance of the indent from the phase boundary.

In order to correlate the indentation response with the locally induced stresses during the thermomechanical pre-treatment, residual stress measurements were performed across the same BCC-FCC phase boundary, enclosed in Area 1. Fig.5a shows a panoramic image of the milled slit overlaid with the displacement field measured from DIC. The shown image is a superposition of 5 SEM images acquired at higher magnifications and subsequently stitched in series. The images were captured with 20% overlap to ensure no loss of spatial data. The displacements represented by colors between green and red indicate displacements along the positive x direction, while those towards blue represent displacements towards the negative x direction. The measured displacement values vary from ~ -25 nm to ~36 nm. The FCC-BCC interface is marked by the yellow arrow, corresponding to the phase boundary close to which the indents were made (c.f. Fig.3). The LAM and geometrically necessary dislocation densities (ρ_{GND}) obtained from EBSD data are plotted as a function of

longitudinal distance along the slit in Fig.5b. ρ_{GND} values were obtained from the EBSD data using the classical strain gradient approach [27,28], given by the following expression,

$$\rho_{GND} = \frac{2\theta}{n\lambda|\boldsymbol{b_d}|} \ldots (2)$$

where, θ is the experimentally measured KAM value, λ is the step size, n is the number of nearest neighbors averaged in the KAM calculation and $\boldsymbol{b_d}$ is the Burgers vector corresponding to the active slip system in the grain. The excellent agreement between the LAM and ρ_{GND} values is not surprising since both values are derived from the measured local misorientation. The region labelled as BCC-HEA grain represents both disordered A2 and ordered B2 phases [20], whereas the FCC-HEA grain corresponds to the FCC phase (c.f. Fig.5b). The interphase highlighted by yellow arrow in Fig.5a and renamed as *Phase boundary I* in Fig.5b corresponds to the same boundary shown in Fig.3c. *Phase boundary II* corresponds to the BCC-FCC interphase boundary on the opposite end of the BCC grain (not visible in Fig.5a). Both LAM and dislocation densities indicate a sharp discontinuity at the FCC-BCC interphase. The dislocation densities in the BCC grain show a peak close to the boundary and steadily decrease with increasing distance from the phase boundary. In the grain interior, the values show local fluctuations. The FCC phase shows a local minimum close to the phase boundary succeeded by a gradual decline in the local dislocation density values on moving away from the phase boundary. Site specific stress measurements shown in Fig.5c correlate extremely well with the EBSD misorientation data validating the physical significance of the observed trends. The measured stress component is normal to the slit length and nearly parallel to the grain boundary plane separating BCC and FCC grains. The stresses in the BCC grain interior are compressive with local stress magnitudes reaching close to 300 MPa. These transition into low magnitude tensile stresses near the interface (c.f. Fig.5c). On the other hand, the stress values in the FCC grains are of compressive

nature, with a stress minimum appearing very close to the interface. The horizontal error bar signifies the spatial resolution of the measurement that is calculated as 0.29 μm.

Easy slip transfer

The BCC-FCC interface enclosed in Area 2 (Figs.2a and 2c) indicated easy slip transfer with a calculated $m' = 0.9$. Load-displacement curves corresponding to indents performed at and near BCC-FCC grain boundary: in the BCC (600 nm from the boundary) as well as the FCC (553 nm from the boundary) grains are shown in Fig.6a. On comparing the three indents, it can be seen that the peak load progressively drops as the indent location moves from the BCC grain to the FCC grain, with peak load values for indentation at the boundary lying in between the two. Fig.6b shows a magnified image of the initial regime of the load-displacement data for the indents shown in Fig.6a. Yielding in the BCC grain displayed staircase characteristics as reported in ref. [20]. The deviation of the load-displacement curve from Hertzian behavior, for the indent made in the BCC grain is marked by appearance of a pop-in of width ~ 2 nm (shown by green arrow in Fig. 6b). In case of the FCC phase, elastic to plastic transition was marked by a yield excursion of magnitude ~4 nm. Secondary strain bursts of comparable size as the initial elastic-to-plastic pop-in were observed at indentation depths of ~15 nm in FCC (large blue arrow in Fig.6b) and at ~20 nm in BCC (large green arrow in Fig.6b) grains. This was subsequently followed by multiple small scale pop-in events. Indentation at the boundary showed the onset of plasticity immediately, with no distinct elastic loading regime (see black arrows highlighting absence of elastic loading response). Further loading did not reveal any distinct displacement burst events, apart from randomly occurring small scale pop in events.

Fig.7 represents the internal stress gradients measured across the BCC-FCC interphase boundary enclosed in Area 2. Fig.7a shows the SE imaging overlaid with displacement field

map obtained from DIC. Fig.7b shows the variation of LAM and ρ_{GND} values over the slit length. Unlike Fig.5b, the values indicate a smooth transition across the BCC-FCC interface labelled as *Phase boundary I*. The dislocation density profile in the FCC grain shows a non-monotonic behavior, highlighted by a local minimum appearing within first 300 nm from the interface (see shaded region in Fig.7b). The corresponding residual stress profile in Fig.7c agrees well with the misorientation and dislocation density variation trends. The locally stored stresses in the BCC grain interior show large fluctuations with values reaching up to ~ -700 MPa.

4. Discussion

The present work investigates intrinsic size effects on the nanomechanical response near the BCC-FCC interfaces in $Al_{0.7}$CoCrFeNi HEA. In particular, the mechanistic contribution of BCC-FCC interfaces in small scale plasticity in HEAs is gauged.

4.1. Strain transfer across BCC-FCC interfaces

The deformation microstructure of the HEA after hot forging was peculiar with respect to the overall heterogeneity in strain distribution between the FCC and BCC grains, with latter bearing most of the strain. Noteworthy is the influence of grain boundary geometry on the strain distribution between the neighboring FCC and BCC grains. When the grain boundaries act as obstacles to dislocation motion, strain transfer into the FCC grain is completely blocked. On the other hand, the boundaries allowing easy strain transfer resulted in profuse slip and substructure formation inside the FCC grain.

In the present alloy indentations performed in the BCC-HEA grain, near the BCC-FCC interface indicate secondary displacement bursts (c.f. Fig. 8) after the initial elastic-plastic yield excursion. These additional yield excursions are associated with release of pile-up stress at the interface, wherein as the stress concentration at the tip of pile-up configuration

exceeds a certain critical value, the dislocations are either directly transmitted across the boundary or first are absorbed into the boundary and subsequently emitted into the neighboring grain [12,29]. The feasibility of dislocation absorption into the grain boundary largely depends upon the nature of stress fields generated during interaction of pile dislocations and the grain boundary dislocations [30–32]. With regards to the dislocation emission, the possible mechanisms could be either by means of slip propagation (wherein availability of a geometrically aligned active slip system in the neighboring grain is a pre-requisite) or by nucleation of dislocations, either at the boundary or in the neighboring grain [12,29,30]. Theoretically, it is expected that the more favorable pathway will be the one associated with minimum energy expenditure. In that respect, the former mechanism of direct slip propagation will be preferred for the case of easy slip transfer (i.e. *Area 2*), whereas for grain boundaries severely blocking dislocations (i.e. *Area 1*) emission via. dislocation nucleation mode (i.e. at grain boundary or in the neighboring FCC grain) is the only available means for releasing pile-up stress.

The appearance of more than one grain boundary related pop-ins for indents made in Area 1 therefore alludes to the mechanism of the absorption of BCC lattice dislocations into the interphase boundary and subsequent nucleation assisted emission in the FCC grain, when local stress at the grain boundary becomes sufficiently high to nucleate dislocations (corroborated by the rapid hardening observed between zone I and zone II). It is proposed that the release of the pile-up ahead of the grain boundary occurs by absorption of lattice dislocations into the grain boundary and subsequent grain boundary yielding, accounting for the first grain boundary associated strain burst event. Absorption of incoming lattice dislocations should also result in local shear and concurrent rotation of the grain boundary plane [33–35]. Such phenomenon can be observed in Figs. 3a and 9 wherein the boundary segment in the vicinity of the indent (located at 110 nm from the boundary) is slightly

displaced into the FCC grain. Grain boundary misorientation values measured before and after indentation indicate an angular deviation of $\sim 12°$ corresponding to the displaced boundary segment. Interestingly the measured grain boundary shear induced by the pile-up (c.f. Fig.9) results in a coupling factor [36] $\theta_{coupling} \sim 12.7°$, which further validates the hypothesis of shear induced grain boundary motion due to absorption of lattice dislocations.

Dislocation emission into the FCC grain occurs by means of dislocation nucleation at the grain boundary rather than taking place in the FCC grain interior. In this respect, the grain boundary ledges or steps created during the shearing process can facilitate dislocation nucleation at the grain boundary at significantly lower stresses compared to the homogeneous nucleation stress [29]

An estimate of the critical stress $'\tau_{crit}'$ at which dislocation emission initiates in the neighboring grain can be extracted from the instantaneous hardness value at the grain boundary just prior to the second grain boundary related burst, giving a value of $\sim 4\ GPa$ for the indent located at 110 nm from the boundary (approx. one-sixth of the measured CSM hardness). Comparing this value to the magnitude of stress for homogenous nucleation in the FCC grain interior i.e. the theoretical shear strength, which is $\sim 12 - 15\ GPa$, indicates a much easier nucleation scenario in grain boundary than grain interior, thereby validating the aforementioned argument.

On the other hand, the resolved shear stress for plasticity initiation in the BCC grain for the same indent (c.f. Fig. 8) i.e. stress at the onset of the first observed pop-in, is calculated as $\tau_{RSS} = 2.4\ GPa$ ($P_{pop\text{-}in}$ = 0.0075 mN; $\tau_{RSS} = \left(\frac{0.47}{\pi}\right)\left(\frac{4E^*}{3R}\right)^{2/3} P^{1/3}$; R is the effective Hertzian contact radius and E^* is the reduced modulus obtained from indentation data [37,38]). It must be noted that the resolved shear stress for plasticity initiation in the same BCC grain interior (in a region far away from the influence of boundary) was determined in

the range of $4.7 - 5.6\,GPa$ [20]. A relatively lower resolved shear stress in the vicinity of the BCC-FCC interface is owing to a pre-strained matrix, whereby dislocation densities close to the boundary can be order of magnitude larger than those in the grain interior (c.f. Fig.5b). The values indicate that the critical stress for dislocation transfer to neighbor grain is greater than the resolved shear stress at which the BCC grain interior locally yields, thereby elucidating the obstacle strength of the grain boundary against dislocation motion. The determined values implicate the dual role of grain boundaries in acting as obstacles as well as dislocation sources.

Indentations performed near the BCC-FCC interface enclosed in *Area 2* displayed multiple pop-in events (Fig.6) of magnitudes significantly smaller than the ones observed in BCC. The observed pop-ins most likely indicate strain transfer by repetitive instances of absorption and emission via direct slip transmission into the neighboring grain. Since the grain boundary resistance against slip is expected to be small, formation of pile-up stresses will be unfavorable whereby excursions associated with grain boundary plasticity will initiate at lower stresses. Subsequently after each excursion, the indenter moves in rapidly by a distance equal to the burst magnitude and the local applied stress drops abruptly. It is likely that this decrement can result in the local stress state to transition into an elastic loading scenario, whereby subsequent load increment would be required to reinitiate plasticity, thus explaining the staircase flow behavior [29].

Nanomechanical response at the BCC-FCC interphase boundary differed from indentations made near the boundary in terms of virtual absence of an elastic loading regime. The observations imply the highly disordered structure of the grain boundary, wherein lack of long range crystallinity makes nucleation of plasticity easier. The findings also agree with the aforementioned predictions of easier dislocation nucleation at the boundary than the bulk. The mechanical response of phase boundary shows a composite like behavior with the

peak load and hardness values lying in between the hard BCC grain and the soft FCC grain [18,19].

4.2. Residual stress gradients and local strengthening response

Residual stress gradients across the BCC–FCC grain boundary in *Area 1* was marked by a sharp discontinuity on moving from the BCC to FCC, highlighting the influence of the interfaces that block strain transfer on the local strain partitioning behavior. On the other hand, stress profiles associated with interface enclosed in *Area 2* showed a smooth transition, displaying no stress discontinuity across the BCC-FCC interphase boundary. Stress values inside the BCC grain indicate significant fluctuations most likely owing to large inherent lattice distortions expected in HEAs as well as the presence of compositionally ordered and disordered BCC phases. In case of the FCC grains, a stress minimum is exhibited at distances within ~ 0.3 μm from the interface, thereby deviating from the typical monotonic stress decrement defined by the Hall-Petch type relationship. Fig.10 shows site specific residual stress and hardness variation with distance from the BCC-FCC interface, indicating an inverse correlation between the two strengthening parameters. It is proposed that the aforementioned observations arise from the role of interface-dependent strengthening mechanisms associated with heterophase interfaces.

In accordance with continuum dislocation pile-up theory, the obstacle strength exerted by the interphase boundary at the tip of the pile up can be described by the well-known formulation given by Eshelby, Frank and Nabarro (EFN) [39], given as

$$\sigma_y = \sigma_0 + \left[\frac{Gb(1-\nu)\tau_a}{\pi L}\right]^{0.5} \quad (3)$$

where σ_y is the yielding stress, σ_0 is the lattice friction stress, G is shear modulus, ν is Poisson's ratio, L is the pile-up length and τ_a is the minimum stress to overcome the barrier

resistance to slip motion. The second term on the right hand side in Eqn. 3 can be further re-written as,

$$kL^{-0.5} = \left[\frac{Gb(1-\nu)\tau_a}{\pi L}\right]^{0.5} \quad (4)$$

where, k is also known as the Hall-Petch coefficient that correlates interfacial yield strength to dislocation pile-up length. By empirically fitting the measured local residual stress values in the BCC grain (c.f. Fig. 5c) as a function of square root of distance from the interface, the experimental value of k for the interface in Area 1 is calculated as $0.145\ MPa.m^{0.5}$. Substituting this value of k to Eqn. 4 gives the value of τ_a as ~ $1.8\ GPa$. Comparing this to the critical stress for dislocation emission in neighboring FCC grain (c.f. Section 4.1) shows a large discrepancy ($\tau_{crit} \approx 4\ GPa$ vis-à-vis $\tau_a \sim 1.8\ GPa$), thereby indicating the presence of unaccounted contributions of additional interface-dependent dislocation strengthening mechanisms.

Strengthening in heterophase interfaces, such as BCC-FCC phase boundary, involves contributions from primarily three mechanisms viz. modulus mismatch, lattice parameter difference and stacking fault differential between adjacent phases. The modulus mismatch or the Koehler barrier introduces a force between a dislocation and its image in the interface. The lattice parameter mismatch generates coherency stresses in case of coherent interfaces and van der Merwe misfit dislocations at or near the interfaces that are incoherent, which interact with incoming lattice dislocations. The stacking fault differential introduces a localized force on gliding dislocations due to core energy changes at or near the interfaces. More precisely, considering the contribution of interface-dependent strengthening mechanisms, the overall interface barrier strength $'\tau_{int}'$ could be mathematically expressed as,

$$\tau_{int} = \tau_a + \tau_K + \tau_{misfit} + \tau_{ch} \quad (5)$$

Where, τ_a is the interface independent barrier strength determined from EFN or Hall-Petch formulation; τ_K is the contribution from image forces or Koehler stresses; τ_{misfit} is due to lattice mismatch and τ_{ch} results from stacking fault mismatch between the two phases. The image force τ_K resulting from interaction of a single screw dislocation with an interface barrier or free surface can be roughly expressed as [40],

$$\tau_K = \frac{G_A(G_B - G_A)}{4\pi(G_B + G_A)} \cdot \frac{b}{h} \quad (6)$$

Where, G_A and G_B are the shear moduli values of incident and emission grains, respectively; b is the magnitude of Burgers vector of active slip system in incident grain; h is the normal distance between dislocation and interface. The sign of the exerted image force influences the nature of interaction between incoming lattice dislocations and the interface. Typically a dislocation near the interface will exert a strain field in both the grains. In case of a shear moduli anisotropy given as, $G_A > G_B$; the dislocation energy in the stiffer grain A will be larger per unit dislocation length. Hence, in order to reduce the energy of the system a dislocation in the softer grain B will be repelled by the interface ($\tau_K > 0$), while the dislocation in grain A will experience an attractive image force ($\tau_K < 0$) [29-32].

Eqn. 6 describes the image force due to presence of a single dislocation at distance h from the interface. In case of a pile-up near the boundary, each dislocation in the pile-up will give contribute to the net image force generated at the interface. This implies that the spearhead dislocation will experience an image force due to itself as well as the overall stress field generated by $n_{pu} - 1$ dislocations lying behind it (where n_{pu} is the number of dislocations in a pile-up). On the other hand, considering that the value of τ_K varies inversely with the distance from interface, it can be safely assumed that the image force component

due to leading dislocation will be far greater than the contribution from neighboring pile-up dislocations. Assuming the minimum possible distance between a lattice dislocation and a grain boundary dislocation is $h_{min} = 2b$, Eqn. 6 gives the maximum image force τ_K^{max} experienced by the leading dislocation as, $\tau_K^{max} = \frac{(G_B - G_A)}{4\pi(G_B + G_A)} \cdot \frac{G_A}{2}$. In the present case the elastic modulus of the BCC-HEA grain is larger than the FCC-HEA grain, as measured by indentation ($E_{BCC-HEA}^{indentation} = 275\ GPa$ vis-à-vis $E_{FCC-HEA}^{indentation} = 252\ GPa$). It is worthwhile to mention that such a modulus differential is unlike that observed in conventional BCC and FCC lattices, wherein the latter typically possesses higher stiffness due to more efficient atomic packing. The opposite trend in the current work most likely alludes to the contribution of ordered B2 phases present in the BCC grain on the overall elastic modulus [20]. Determining the shear moduli from the above values using $G = E/2(1 + \nu)$, the image force τ_K experienced by a screw dislocation at the tip of the pile-up in the BCC-HEA grain is determined as $-191\ MPa$. In the case of edge dislocations the values of τ_K also lie in a similar range. Using a similar approach the image force experienced by a FCC-HEA dislocation due to the interface can be estimated as $+168\ MPa$.

The sign of the image force indicates the favorability of absorption and core spreading of BCC lattice dislocations into the interface, corroborating the slip transfer mechanism involving shear coupled grain boundary migration, as elucidated in Section 4.1. On the other hand, FCC dislocations will be repelled by the interface, resulting in local increase in hardness, since the generated dislocations are unable to move away from the indent towards the grain boundary. This also explains the local decrease in dislocation densities in the vicinity of the grain boundary and appearance of local minimum in internal stress values observed for the FCC grain (c.f. Figs 5b-c, 7b-c and 10). Note that appearance of such local

stress minimum is not seen for the BCC grain (c.f. Figs 5b-c, 7b-c and 10), wherein the image forces exert an attractive pull on the grain boundary.

Interfacial strengthening in BCC-FCC interfaces in the present HEA, also derive contributions from lattice parameter mismatch and stacking fault difference, expressed mathematically as Eqns. 7 and 8 [40,41],

$$\tau_{misfit} = 0.5G^{*}\sqrt{\frac{2b(\delta-\varepsilon)}{\lambda}} \quad (7)$$

$$\tau_{ch} = \frac{\Delta\gamma}{b} \quad (8)$$

where, $\delta = {\Delta a}/{\bar{a}}$; $\bar{a}$ is the mean lattice parameter $(a_{BCC} + a_{FCC})/2$, $\varepsilon = 0.76\delta$ is the residual elastic strain determined that was shown to agree for most heterophase interface types [41], G^{*} is the average shear modulus for the two phases, λ is the grain dimension over which misfit stresses are determined (in the present case the indent to interface distance), and $\Delta\gamma$ is the stacking fault energy (SFE) differential between neighboring phases. The lattice parameters of the present BCC-HEA and FCC-HEA grains are $0.28905\,nm$ and $0.36048\,nm$, respectively [41]. This gives a misfit value of $\delta = 0.22$. The value of b in the BCC grain is $\sim 0.25\,nm$. Substituting these values in Eqn. 7 and assigning λ as 110nm (corresponding to the 2nd nearest indent location in BCC grain from the interface highlighted in Fig.9), the misfit stress τ_{misfit} resulting from BCC-FCC interface in $Al_xCoCrFeNi$ HEA is given as $0.82\,GPa$.

It is well established that SFE values in BCC HEAs are significantly larger than FCC HEAs. Though the literature does not report SFEs specifically for $Al_xCoCrFeNi$ HEAs, an estimate of the order of mismatch can still be made using the SFE values derived from atomistic simulations performed for FCC and BCC type HEA lattices by Rao and co-

workers [42,43]. They reported SFE values of BCC-HEAs in the range of 380-418 mJ.m^{-2} [42] and for FCC-HEAs the values were around 20-40 mJ.m^{-2} [43,44]. The corresponding stacking fault strengthening across BCC-FCC interfaces is then calculated using Eqn. 8, as $\sim 1.4 - 1.6\ GPa$.

Using Eqn. 5, the overall interfacial resistance τ_{int} experienced during slip transfer from the BCC grain to FCC grain is estimated to be in the range of $\sim 3.8 - 4\ GPa$, which is in excellent agreement with experimentally determined value of τ_{crit} for the indent located at 110 nm from the interface, as determined from CSM indentation hardness data (c.f. section 4.1). In contrast to conventional BCC-FCC interfaces that typically exhibit τ_{int} values in the range of $\sim 0.3 - 1.1\ GPa$, the values in the present HEA is nearly 4 times larger. These values allude to the presence of significantly more complex local atomic interactions and strain compatibility mechanisms in multicomponent alloys in comparison with conventional materials.

Fig.10 also indicates that for larger compressive residual stresses the recorded hardness values are also higher. Theoretically, it can be shown that in case of uniaxial tensile residual stresses the maximum shear stress beneath the indenter constructively superposes with the local tensile stress fields. On the other hand, a uniaxial compressive stress field will negligibly influence the maximum shear stress component underneath the indenter since both stress components lie on entirely different planes [45,46]. The scenario however changes under a bi-axial stress state, wherein the asymmetry in the hardness variation under tensile and compressive residual stress states is not observed [45]. Fig. 10 indicates stresses only along one of the lateral directions i.e. *x*-direction as shown in Figs. 5 and 7. In order to estimate the overall in-plane stress state, stresses were also calculated along the *y*-direction, by milling a slit oriented along *x*-direction inside the BCC grain. The measured stress was tensile, given as σ_{y-mean} ~ 60 MPa. Considering the *x* and *y*-axes to be the principal stress

directions an estimate of the local average normal stress/ hydrostatic component at each indent location $'n'$ can be approximated as, $\sigma_n = \frac{(\sigma_x^n + \sigma_{y-mean})}{2}$; where σ_x^n is the measured residual stress along x-direction at location n, as extracted from Fig. 10. Since the values of σ_x^n vary from -100 to - 600 MPa, σ_n assumes a compressive stress value, thereby indicating that the material beneath the indenter experiences an in-plane biaxial compressive stress state. This explains the strong dependence of hardness values on the compressive residual stress state in Fig. 10, which contradicts the predicted hardness response under uniaxial compressive residual stress fields.

With respect to fracture response a tensile stress and low hardness value at the interphase would promote preferential crack nucleation and propagation along the boundaries in $Al_{0.7}$CoCrFeNi HEAs, as depicted in Fig.11, wherein an indentation performed at higher loads near a BCC-FCC phase boundary leads to crack propagation along the interphase. The outcomes and trends highlight the crucial role of interphase boundary crystallography and pre-strain on the subsequent mechanical response and damage behavior not only across $Al_{0.7}$CoCrFeNi interphase boundaries but also with regards to generic BCC-FCC interfaces existing in conventional alloys.

5. Conclusions

Nano indentation induced plasticity and local residual stress gradients were correlated to assess the local mechanical and damage response of BCC-FCC interfaces in multiphase HEAs. The following key conclusions were derived:

I. Blocking strength of interfaces was attributed to the sum total effect of interfacial-dependent and independent strengthening mechanisms. In case of BCC-FCC interface in Al_xCoCrFeNi HEA, an overall interfacial strengthening stress was estimated to be

$\sim 3.8 - 4\ GPa$, being ~ 4 times larger than the values seen for conventional BCC-FCC interfaces.

II. BCC dislocations experience attractive image forces such that they are absorbed into the interphase boundary and subsequently result in a local drop in nano-hardness values near the interface. Image forces on the FCC side were repulsive, whereby FCC lattice dislocations are repelled by the interface resulting in a local minimum in stress values very close to the boundary. The reverse trend is observed for the nano-hardness values close to the interface, since the generated dislocations are unable to glide away from indented region.

III. Local stresses strongly determine the hardness response as indicated by lower hardness values in regions of low compressive/tensile stresses and higher hardness values in the regions of high compressive stress. The BCC-FCC interphase boundaries acted as the weak spots with fracture initiation preferably occurring along the grain boundary.

Acknowledgments

This research was carried out under project number T61.1.14545 in the framework of the Research Program of the Materials innovation institute (M2i) (www.m2i.nl). The authors also acknowledge Prof. P.K. Liaw for providing material for the study.

References

[1] J.-W. Yeh, Alloy Design Strategies and Future Trends in High-Entropy Alloys, JOM. 65 (2013) 1759–1771. doi:10.1007/s11837-013-0761-6.

[2] M.C. Gao, J.-W. Yeh, P.K. Liaw, Y. Zhang, High-Entropy Alloys: Fundamentals and Applications, Springer, 2016.

[3] B. Cantor, I.T.H. Chang, P. Knight, A.J.B. Vincent, Microstructural development in equiatomic multicomponent alloys, Mater. Sci. Eng. A. 375–377 (2004) 213–218. doi:10.1016/j.msea.2003.10.257.

[4] D.B. Miracle, O.N. Senkov, A critical review of high entropy alloys and related concepts, Acta Mater. 122 (2017) 448–511. doi:10.1016/j.actamat.2016.08.081.

[5] J.C. Rao, H.Y. Diao, V. Ocelík, D. Vainchtein, C. Zhang, C. Kuo, Z. Tang, W. Guo, J.D. Poplawsky, Y. Zhou, P.K. Liaw, J.T.M. De Hosson, Secondary phases in AlxCoCrFeNi high-entropy alloys: An in-situ TEM heating study and thermodynamic appraisal, Acta Mater. 131 (2017) 206–220. doi:10.1016/j.actamat.2017.03.066.

[6] Z. Tang, O.N. Senkov, C.M. Parish, C. Zhang, F. Zhang, L.J. Santodonato, G. Wang, G. Zhao, F. Yang, P.K. Liaw, Tensile ductility of an AlCoCrFeNi multi-phase high-entropy alloy through hot isostatic pressing (HIP) and homogenization, Mater. Sci. Eng. A. 647 (2015) 229–240. doi:10.1016/j.msea.2015.08.078.

[7] Z. Li, C.C. Tasan, H. Springer, B. Gault, D. Raabe, Interstitial atoms enable joint twinning and transformation induced plasticity in strong and ductile high-entropy alloys, Sci. Rep. 7 (2017) 40704. doi:10.1038/srep40704.

[8] S.S. Nene, K. Liu, M. Frank, R.S. Mishra, R.E. Brennan, K.C. Cho, Z. Li, D. Raabe, Enhanced strength and ductility in a friction stir processing engineered dual phase high entropy alloy, Sci. Rep. 7 (2017) 16167. doi:10.1038/s41598-017-16509-9.

[9] C.C. Tasan, D. Raabe, K.G. Pradeep, Y. Deng, Z. Li, Metastable high-entropy dual-phase alloys overcome the strength–ductility trade-off, Nature. 534 (2016) 227. doi:10.1038/nature17981.

[10] W.-R. Wang, W.-L. Wang, S.-C. Wang, Y.-C. Tsai, C.-H. Lai, J.-W. Yeh, Effects of Al addition on the microstructure and mechanical property of AlxCoCrFeNi high-entropy alloys, Intermetallics. 26 (2012) 44–51. doi:10.1016/j.intermet.2012.03.005.

[11] W.A.T. Clark, R.H. Wagoner, Z.Y. Shen, T.C. Lee, I.M. Robertson, H.K. Birnbaum, On the criteria for slip transmission across interfaces in polycrystals, Scr. Metall. Mater. 26 (1992) 203–206. doi:10.1016/0956-716X(92)90173-C.

[12] Z. Shen, R.H. Wagoner, W.A.T. Clark, Dislocation and grain boundary interactions in metals, Acta Metall. 36 (1988) 3231–3242. doi:10.1016/0001-6160(88)90058-2.

[13] T.C. Lee, I.M. Robertson, H.K. Birnbaum, Interaction of dislocations with grain boundaries in Ni3Al, Acta Metall. Mater. 40 (1992) 2569–2579. doi:10.1016/0956-7151(92)90326-A.

[14] J.S. Koehler, Attempt to Design a Strong Solid, Phys. Rev. B. 2 (1970) 547–551. doi:10.1103/PhysRevB.2.547.

[15] A.K. Head, X. The Interaction of Dislocations and Boundaries, Lond. Edinb. Dublin Philos. Mag. J. Sci. 44 (1953) 92–94. doi:10.1080/14786440108520278.

[16] F.C. Frank, J.H.V.D. Merwe, One-dimensional dislocations. II. Misfitting monolayers and oriented overgrowth, Proc R Soc Lond A. 198 (1949) 216–225. doi:10.1098/rspa.1949.0096.

[17] V. Vitek, Theory of the core structures of dislocations in BCC metals, Cryst Lattice Defects. 5 (1974) 1–34.

[18] J. Wang, A. Misra, An overview of interface-dominated deformation mechanisms in metallic multilayers, Curr. Opin. Solid State Mater. Sci. 15 (2011) 20–28. doi:10.1016/j.cossms.2010.09.002.

[19] Q. Zhou, P. Huang, M. Liu, F. Wang, K. Xu, T. Lu, Grain and interface boundaries governed strengthening mechanisms in metallic multilayers, J. Alloys Compd. 698 (2017) 906–912. doi:10.1016/j.jallcom.2016.12.254.

[20] I. Basu, V. Ocelík, J.T.M. De Hosson, Size dependent plasticity and damage response in multiphase body centered cubic high entropy alloys, Acta Mater. 150 (2018) 104–116. doi:10.1016/j.actamat.2018.03.015.

[21] R. Hielscher, H. Schaeben, A novel pole figure inversion method: specification of the MTEX algorithm, J. Appl. Crystallogr. 41 (2008) 1024–1037. doi:10.1107/S0021889808030112.

[22] W.C. Oliver, G.M. Pharr, Measurement of hardness and elastic modulus by instrumented indentation: Advances in understanding and refinements to methodology, J. Mater. Res. 19 (2004) 3–20. doi:10.1557/jmr.2004.19.1.3.

[23] C. Mansilla, D. Martínez-Martínez, V. Ocelík, J.T.M. De Hosson, On the determination of local residual stress gradients by the slit milling method, J. Mater. Sci. 50 (2015) 3646–3655. doi:10.1007/s10853-015-8927-y.

[24] I. Basu, V. Ocelík, J.T.M. De Hosson, Measurement of spatial stress gradients near grain boundaries, Scr. Mater. 136 (2017) 11–14. doi:10.1016/j.scriptamat.2017.03.036.

[25] I. Basu, V. Ocelík, J.T.M. De Hosson, Experimental determination and theoretical analysis of local residual stress at grain scale, in: WIT Trans. Eng. Sci., WIT press, 2017: pp. 3–14. doi:10.2495/MC170011.

[26] G. Gottstein, Physical Foundations of Materials Science, Springer Science & Business Media, 2013.

[27] L.P. Kubin, A. Mortensen, Geometrically necessary dislocations and strain-gradient plasticity: a few critical issues, Scr. Mater. 48 (2003) 119–125. doi:10.1016/S1359-6462(02)00335-4.

[28] P.J. Konijnenberg, S. Zaefferer, D. Raabe, Assessment of geometrically necessary dislocation levels derived by 3D EBSD, Acta Mater. 99 (2015) 402–414. doi:10.1016/j.actamat.2015.06.051.

[29] W.A. Soer, K.E. Aifantis, J.T.M. De Hosson, Incipient plasticity during nanoindentation at grain boundaries in body-centered cubic metals, Acta Mater. 53 (2005) 4665–4676. doi:10.1016/j.actamat.2005.07.001.

[30] L. Priester, "Dislocation–interface" interaction — stress accommodation processes at interfaces, Mater. Sci. Eng. A. 309–310 (2001) 430–439. doi:10.1016/S0921-5093(00)01696-8.

[31] J.P. Hirth, The influence of grain boundaries on mechanical properties, Metall. Trans. 3 (1972) 3047–3067. doi:10.1007/BF02661312.

[32] R.C. Pond, D.A. Smith, On the absorption of dislocations by grain boundaries, Philos. Mag. 36 (1977) 353–366. doi:10.1080/14786437708244939.

[33] D. Caillard, F. Mompiou, M. Legros, Grain-boundary shear-migration coupling. II. Geometrical model for general boundaries, Acta Mater. 57 (2009) 2390–2402. doi:10.1016/j.actamat.2009.01.023.

[34] T.J. Rupert, D.S. Gianola, Y. Gan, K.J. Hemker, Experimental Observations of Stress-Driven Grain Boundary Migration, Science. 326 (2009) 1686–1690. doi:10.1126/science.1178226.

[35] F. Mompiou, D. Caillard, M. Legros, Grain boundary shear–migration coupling—I. In situ TEM straining experiments in Al polycrystals, Acta Mater. 57 (2009) 2198–2209. doi:10.1016/j.actamat.2009.01.014.

[36] J.W. Cahn, Y. Mishin, A. Suzuki, Coupling grain boundary motion to shear deformation, Acta Mater. 54 (2006) 4953–4975. doi:10.1016/j.actamat.2006.08.004.

[37] K.L. Johnson, Contact Mechanics, Cambridge University Press, 1987.

[38] D.F. Bahr, D.E. Kramer, W.W. Gerberich, Non-linear deformation mechanisms during nanoindentation, Acta Mater. 46 (1998) 3605–3617. doi:10.1016/S1359-6454(98)00024-X.

[39] J.D. Eshelby, F.C. Frank, F.R.N. Nabarro, XLI. The equilibrium of linear arrays of dislocations., Lond. Edinb. Dublin Philos. Mag. J. Sci. 42 (1951) 351–364. doi:10.1080/14786445108561060.

[40] S.I. Rao, P.M. Hazzledine, Atomistic simulations of dislocation–interface interactions in the Cu-Ni multilayer system, Philos. Mag. A. 80 (2000) 2011–2040. doi:10.1080/01418610008212148.

[41] Y.P. Li, G.P. Zhang, W. Wang, J. Tan, S.J. Zhu, On interface strengthening ability in metallic multilayers, Scr. Mater. 57 (2007) 117–120. doi:10.1016/j.scriptamat.2007.03.032.

[42] S.I. Rao, C. Varvenne, C. Woodward, T.A. Parthasarathy, D. Miracle, O.N. Senkov, W.A. Curtin, Atomistic simulations of dislocations in a model BCC multicomponent concentrated solid solution alloy, Acta Mater. 125 (2017) 311–320. doi:10.1016/j.actamat.2016.12.011.

[43] S.I. Rao, C. Woodward, T.A. Parthasarathy, O. Senkov, Atomistic simulations of dislocation behavior in a model FCC multicomponent concentrated solid solution alloy, Acta Mater. 134 (2017) 188–194. doi:10.1016/j.actamat.2017.05.071.

[44] M. Beyramali Kivy, M. Asle Zaeem, Generalized stacking fault energies, ductilities, and twinnabilities of CoCrFeNi-based face-centered cubic high entropy alloys, Scr. Mater. 139 (2017) 83–86. doi:10.1016/j.scriptamat.2017.06.014.

[45] T.Y. Tsui, W.C. Oliver, G.M. Pharr, Influences of stress on the measurement of mechanical properties using nanoindentation: Part I. Experimental studies in an aluminum alloy, J. Mater. Res. 11 (1996) 752–759. doi:10.1557/JMR.1996.0091.

[46] L. Wang, H. Bei, Y.F. Gao, Z.P. Lu, T.G. Nieh, Effect of residual stresses on the hardness of bulk metallic glasses, Acta Mater. 59 (2011) 2858–2864. doi:10.1016/j.actamat.2011.01.025.

CAPTIONS

Fig. 1. Schematic illustrating the methodology for slit-depth determination by site-specific electron beam deposition and focused ion beam milling.

Fig. 2. a) EBSD image quality (IQ) map of $Al_{0.7}CoCrFeNi$ high entropy alloy, with selected phase boundaries (shown by yellow arrows) enclosed in highlighted regions in yellow dotted squares viz. *Area 1* and *Area 2*; Inset image shows phase map differentiating between BCC and FCC grains; b) Kernel Average Misorientation (KAM) on the left and Local Average Misorientation (LAM) on the right side, corresponding to *Area 1* (prior to indentation); indent locations and FIB milled slit geometry is additionally illustrated in the KAM map on the left side; c) Kernel Average Misorientation (KAM) on the left and Local Average Misorientation (LAM) on the right side, corresponding to *Area 2* (prior to indentation); indent locations and FIB milled slit geometry is additionally illustrated in the KAM map on the left side. Phase boundaries are in white and grain boundaries (> 3°) in black.

Fig. 3. a) From left to right: SEM image corresponding to *Area 1* after nano-indentations, magnified view shows elastic strain fields in the vicinity of indents made in BCC that extend into the FCC grain; grain orientation map along with traces of active slip systems (purple (BCC) and mustard (FCC) colored arrows indicate slip direction trace, orange (BCC) and blue (FCC) lines indicate slip plane trace) and experimentally calculated geometrical slip transmission parameter across the probed BCC-FCC interface; grain reference orientation deviation (GROD) map showing indent strain fields, wherein indents lying very close to the boundary (upto ~800nm from boundary) display plastic zones crossing over to the neighboring FCC grain; b) SEM image on right showing the slit orientation with respect to the BCC-FCC interface, image on left magnifies the slit-interface intersection showing the orientation of grain boundary plane with respect to the slit.

Fig. 4. Hardness-depth variation corresponding to indents made far away from the phase boundary and those located at 40nm and 110 nm away from the BCC-FCC interface enclosed in *Area 1*. Zones I and II marked for indent at 40nm from the interface, correspond to appearance of boundary related non-monotonicity in the hardness curves. Black arrows in the same curve indicate the critical depths prior to phase boundary related hardening. Colored arrows indicate the yield excursion events for indents performed near the phase boundary.

Fig. 5. a) DIC contour map showing the displacement fields due to stress release from slit milling in direction lateral to the slit (x-direction), phase boundary enclosed in *Area 1* is marked by the yellow arrow; b) Geometrically necessary dislocation density and local average misorientation gradients in the FCC-HEA and BCC-HEA grains, determined along the slit length (along y-direction); c) Experimentally measured local residual stress lateral to the slit length (along x-direction) plotted with respect to the slit length (along y-direction). FCC-HEA grain shows a local stress minimum and drop in local dislocation density values in the region very close to the BCC-FCC interface as shown by shaded area.

Fig. 6. a) Full load-indentation curves for indents made in the BCC grain and FCC grain, in the vicinity of interface, as well as on the BCC-FCC interphase boundary; b) Magnified view of the curves shown in Fig. 10a with elastic loading regime fitted to Hertzian expression (BCC in black, FCC in red); Major pop-in events (elastic-plastic transition and phase boundary effect) shown by large arrows and smaller pop-ins shown by small sized arrows.

Fig. 7. a) DIC contour map showing the displacement fields due to stress release from slit milling in direction lateral to the slit (x-direction), phase boundary enclosed in *Area 2* is marked by the yellow arrow; b) Geometrically necessary dislocation density and local average misorientation gradients in the FCC-HEA and BCC-HEA grains, determined along the slit length (along y-direction); c) Experimentally measured local residual stress lateral to the slit length (along x-direction) plotted with respect to the slit length (along y-direction). FCC-HEA grain shows a local stress minimum and drop in local dislocation density values in the region very close to the BCC-FCC interface as shown by shaded area.

Fig. 8. Magnified view of load-displacement curves corresponding to indents performed in the BCC-HEA grain at distances 40nm and 110nm from the interphase boundary

Fig. 9. Experimentally measured grain boundary shear induced coupling due to plastic strain generated by an indent performed in the vicinity of the BCC-FCC interphase boundary. Grain on the left is FCC and one on the right is BCC.

Fig. 10. Variation of nano-hardness and local residual stress as a function of distance from the interphase boundary in neighboring BCC and FCC grains

Fig. 11. Experimentally observed fracture initiation along the BCC-FCC interphase boundary for larger indentations (higher imparted total strains).

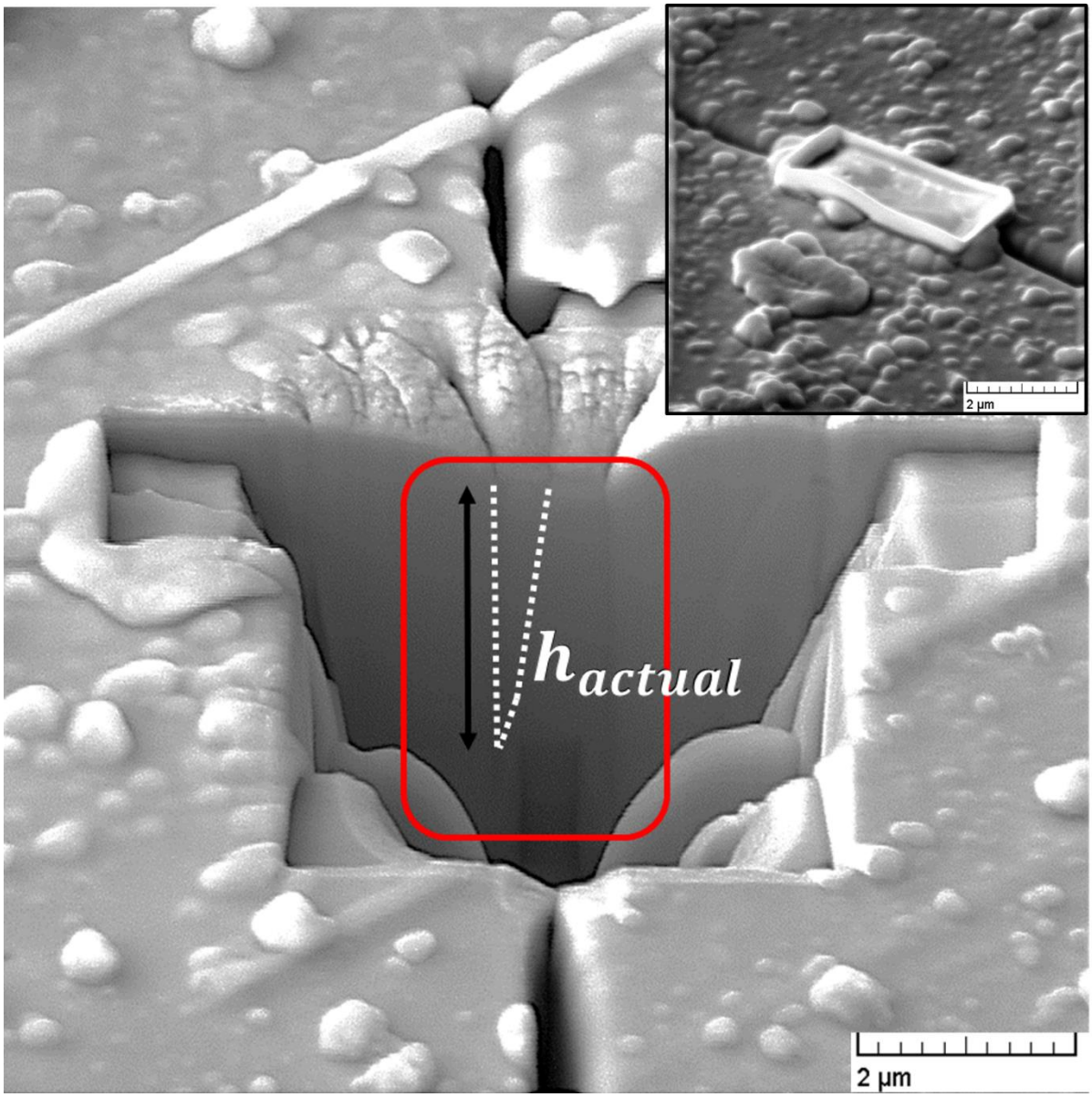

Fig. 1. Schematic illustrating the methodology for slit-depth determination by site-specific electron beam deposition and focused ion beam milling.

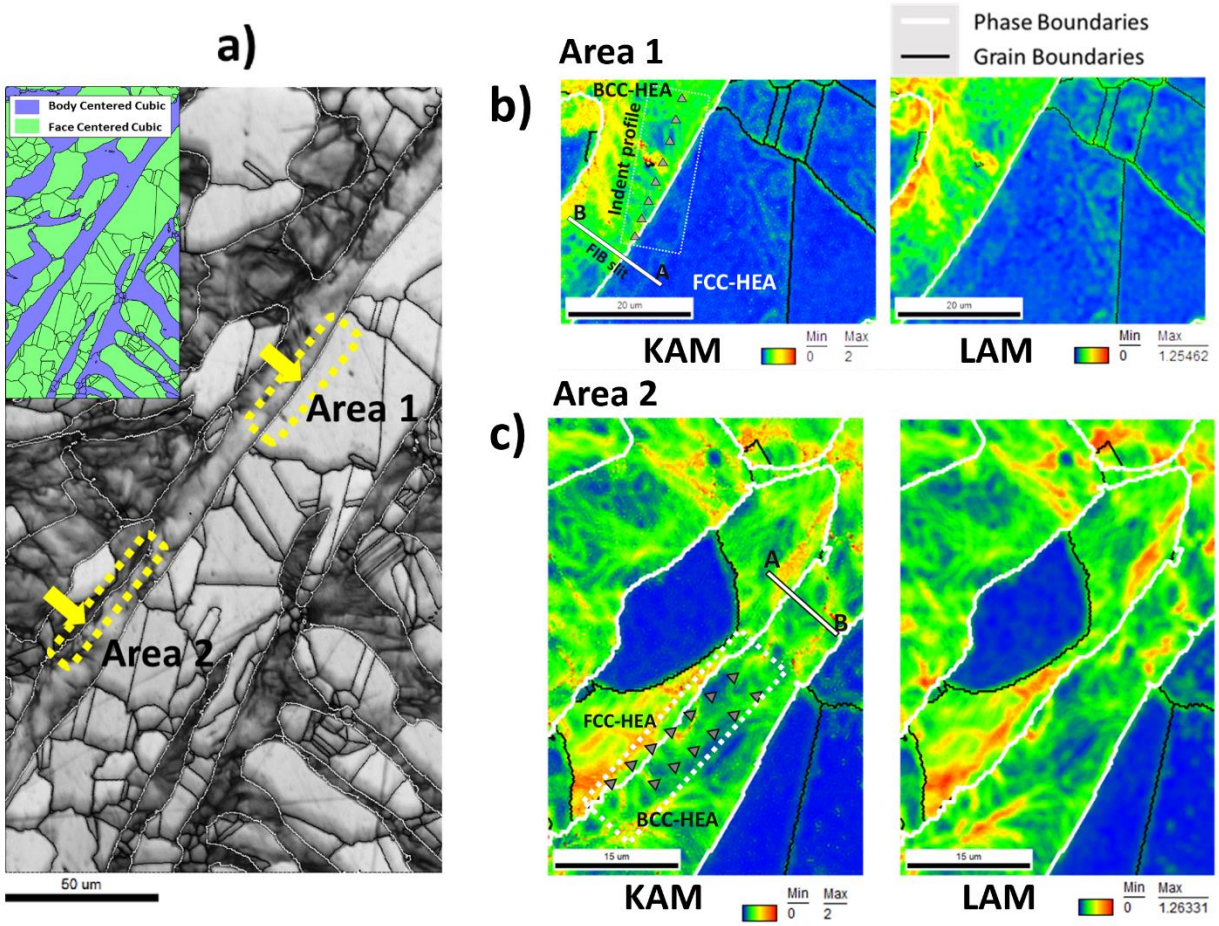

Fig. 2. a) EBSD image quality (IQ) map of $Al_{0.7}CoCrFeNi$ high entropy alloy, with selected phase boundaries (shown by yellow arrows) enclosed in highlighted regions in yellow dotted squares viz. *Area 1* and *Area 2*; Inset image shows phase map differentiating between BCC and FCC grains; b) Kernel Average Misorientation (KAM) on the left and Local Average Misorientation (LAM) on the right side, corresponding to *Area 1* (prior to indentation); indent locations and FIB milled slit geometry is additionally illustrated in the KAM map on the left side; c) Kernel Average Misorientation (KAM) on the left and Local Average Misorientation (LAM) on the right side, corresponding to *Area 2* (prior to indentation); indent locations and FIB milled slit geometry is additionally illustrated in the KAM map on the left side. Phase boundaries are in white and grain boundaries (> 3°) in black.

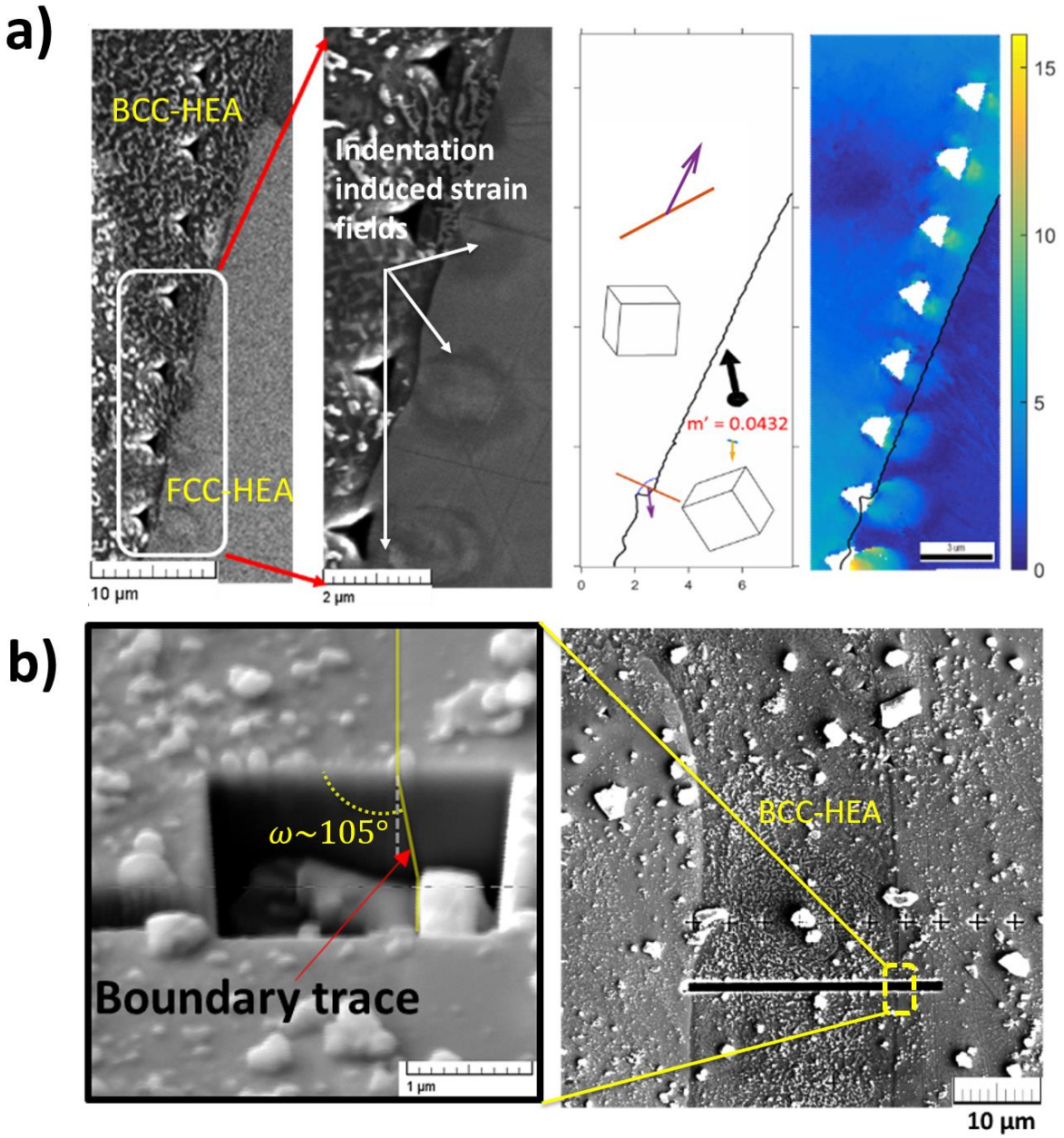

Fig. 3 a) From left to right: SEM image corresponding to *Area 1* after nano-indentations, magnified view shows elastic strain fields in the vicinity of indents made in BCC that extend into the FCC grain; grain orientation map along with traces of active slip systems (purple (BCC) and mustard (FCC) colored arrows indicate slip direction trace, orange (BCC) and blue (FCC) lines indicate slip plane trace) and experimentally calculated geometrical slip transmission parameter across the probed BCC-FCC interface; grain reference orientation deviation (GROD) map showing indent strain fields, wherein indents lying very close to the boundary (upto ~800nm from boundary) display plastic zones crossing over to the neighboring FCC grain; b) SEM image on right showing the slit orientation with respect to the BCC-FCC interface, image on left magnifies the slit-interface intersection showing the orientation of grain boundary plane with respect to the slit.

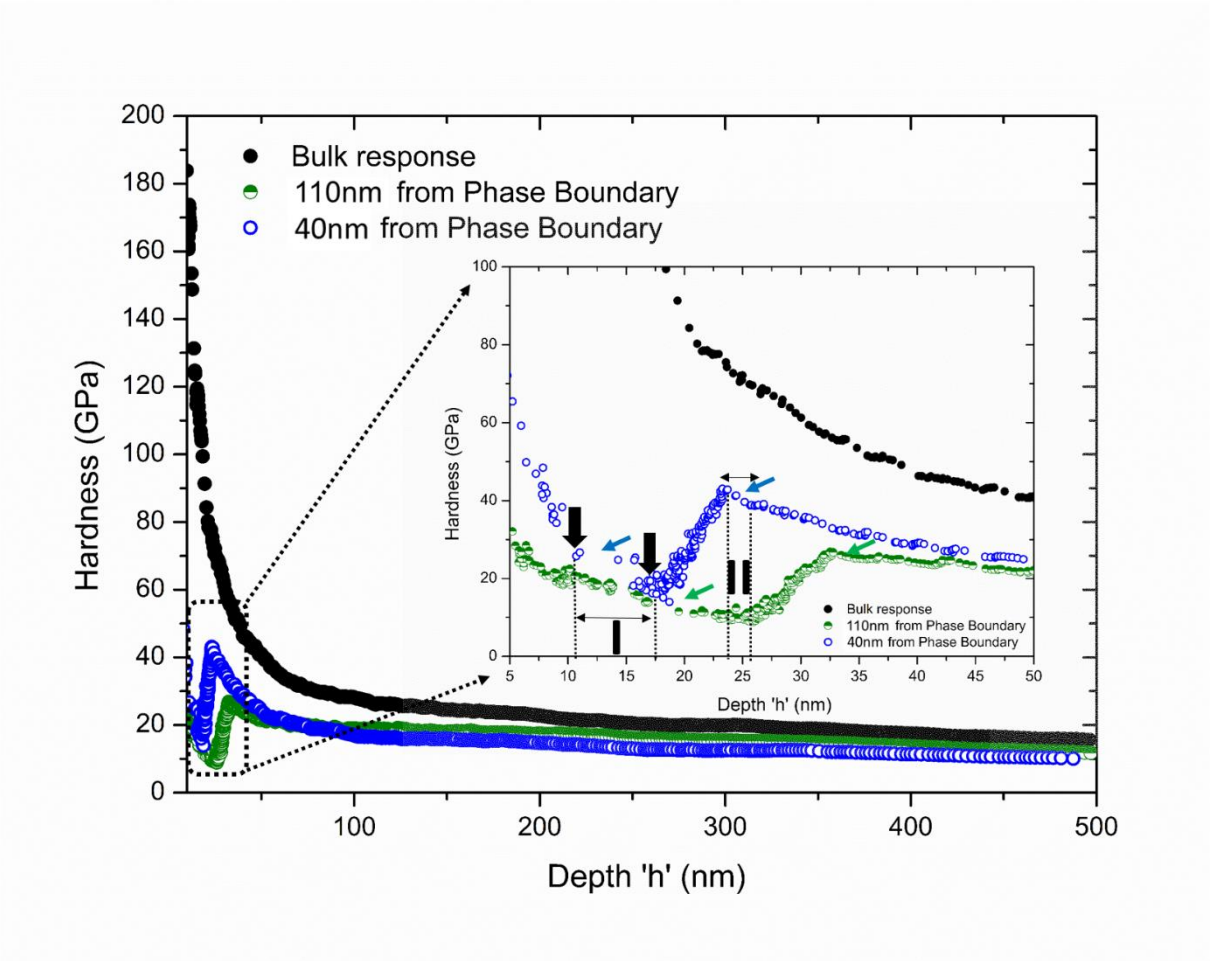

Fig. 4. Hardness-depth variation corresponding to indents made far away from the phase boundary and those located at 40nm and 110 nm away from the BCC-FCC interface enclosed in *Area 1*. Zones I and II marked for indent at 40nm from the interface, correspond to appearance of boundary related non-monotonicity in the hardness curves. Black arrows in the same curve indicate the critical depths prior to phase boundary related hardening. Colored arrows indicate the yield excursion events for indents performed near the phase boundary.

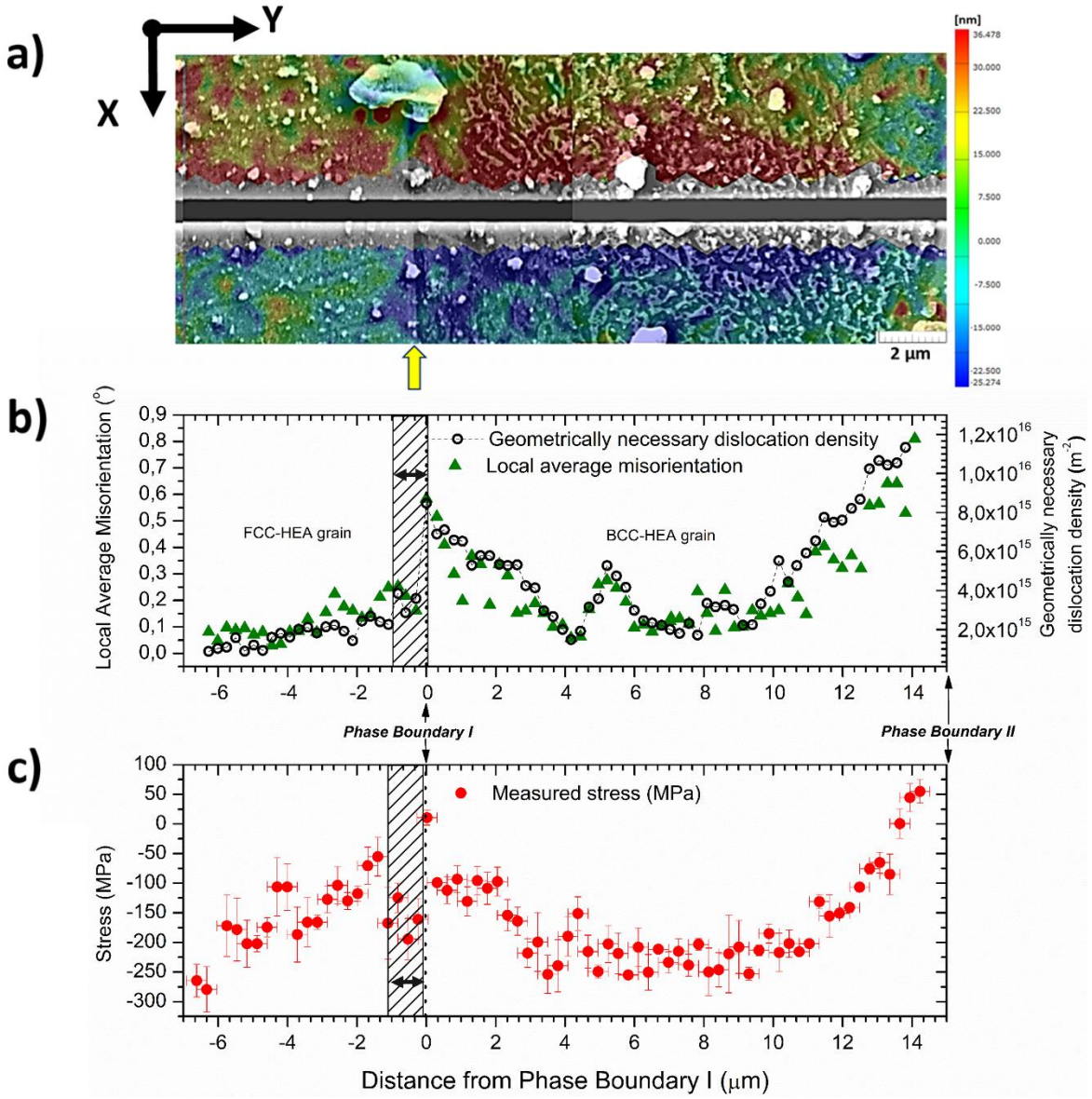

Fig. 5. a) DIC contour map showing the displacement fields due to stress release from slit milling in direction lateral to the slit (x-direction), phase boundary enclosed in *Area 1* is marked by the yellow arrow; b) Geometrically necessary dislocation density and local average misorientation gradients in the FCC-HEA and BCC-HEA grains, determined along the slit length (along y-direction); c) Experimentally measured local residual stress lateral to the slit length (along x-direction) plotted with respect to the slit length (along y-direction). FCC-HEA grain shows a local stress minimum and drop in local dislocation density values in the region very close to the BCC-FCC interface as shown by shaded area.

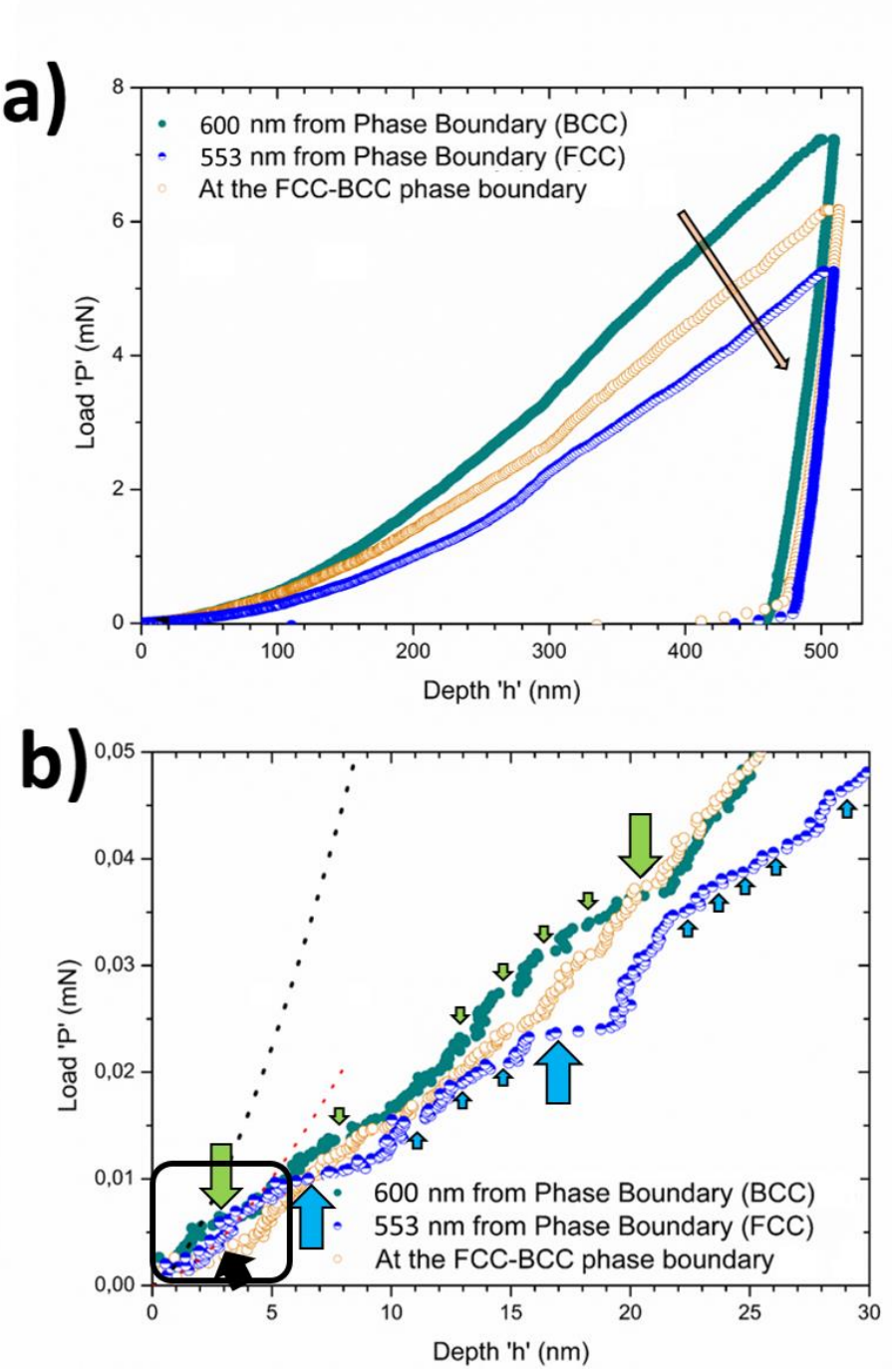

Fig. 6. a) Full load-indentation curves for indents made in the BCC grain and FCC grain, in the vicinity of interface, as well as on the BCC-FCC interphase boundary; b) Magnified view of the curves shown in Fig. 10a with elastic loading regime fitted to Hertzian expression (BCC in black, FCC in red); Major pop-in events (elastic-plastic transition and phase boundary effect) shown by large arrows and smaller pop-ins shown by small sized arrows.

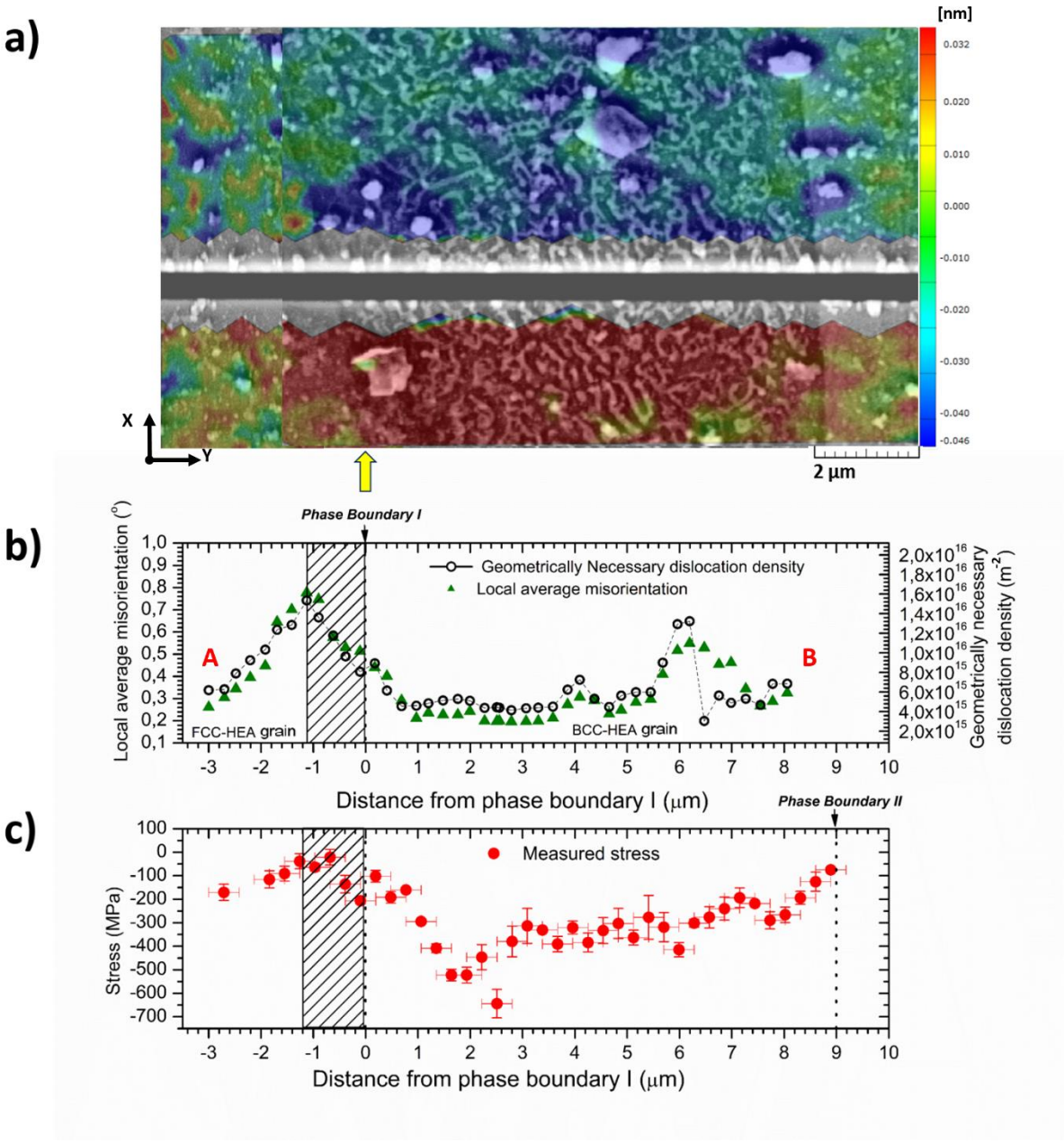

Fig. 7. a) DIC contour map showing the displacement fields due to stress release from slit milling in direction lateral to the slit (x-direction), phase boundary enclosed in *Area 2* is marked by the yellow arrow; b) Geometrically necessary dislocation density and local average misorientation gradients in the FCC-HEA and BCC-HEA grains, determined along the slit length (along y-direction); c) Experimentally measured local residual stress lateral to the slit length (along x-direction) plotted with respect to the slit length (along y-direction). FCC-HEA grain shows a local stress minimum and drop in local dislocation density values in the region very close to the BCC-FCC interface as shown by shaded area.

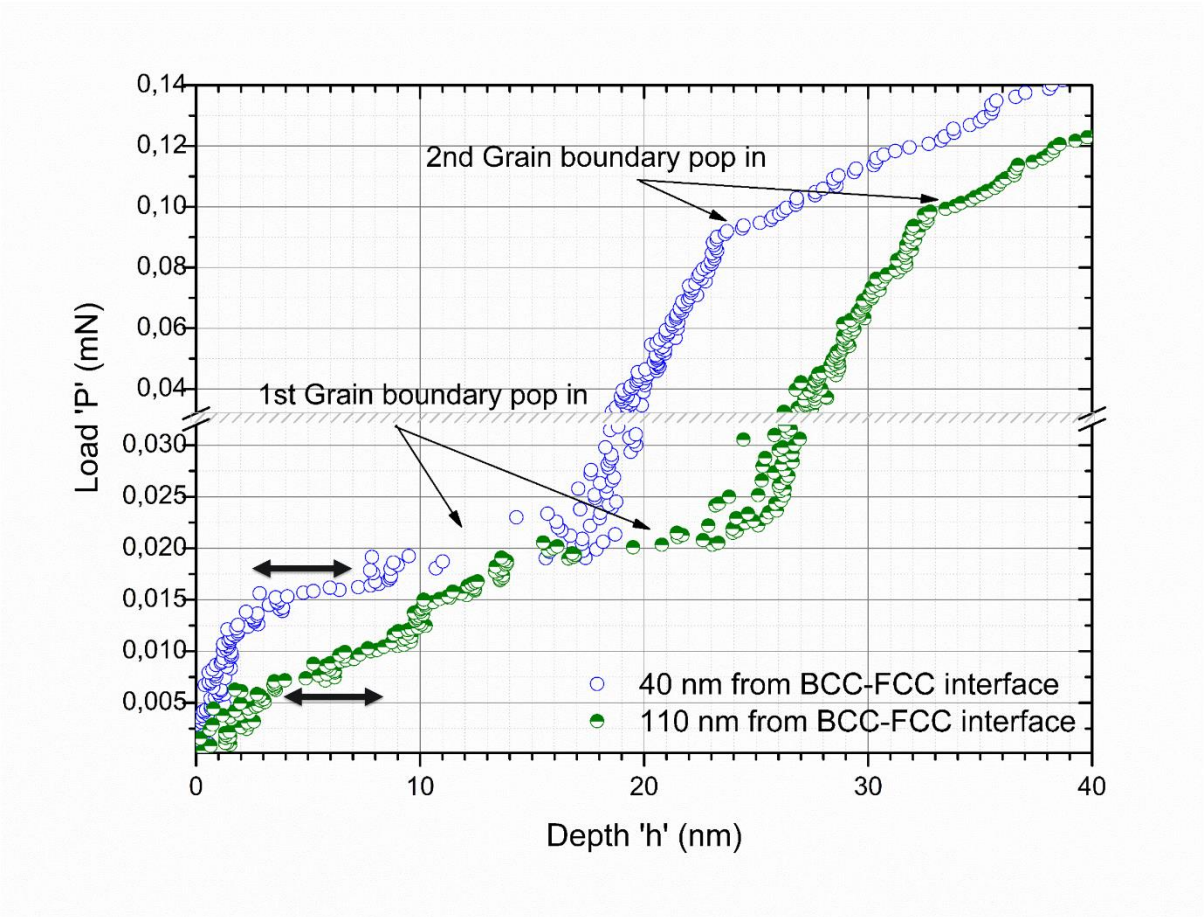

Fig. 8. Magnified view of load-displacement curves corresponding to indents performed in the BCC-HEA grain at distances 40nm and 110nm from the interphase boundary. Double headed arrows indicate the first pop-in event related to the transition from elastic-to-plastic flow behavior.

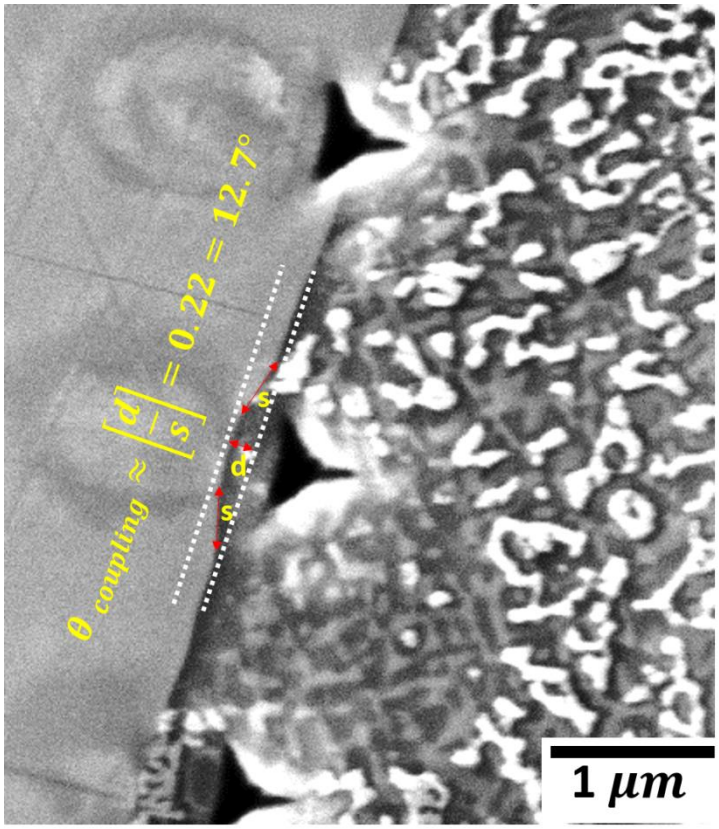

Fig. 9. Experimentally measured grain boundary shear induced coupling due to plastic strain generated by an indent performed in the vicinity of the BCC-FCC interphase boundary. Grain on the left is FCC and one on the right is BCC.

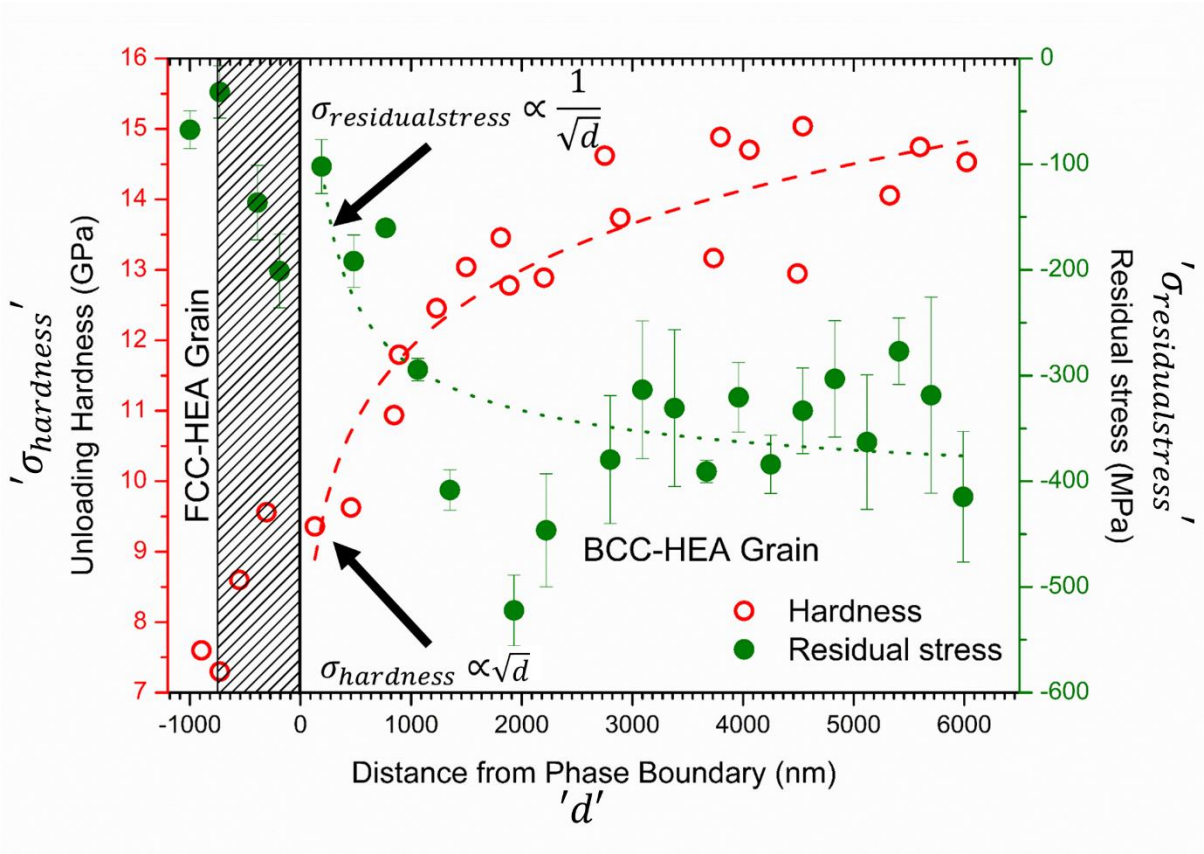

Fig. 10. Variation of nano-hardness and local residual stress as a function of distance from the interphase boundary in neighboring BCC and FCC grains

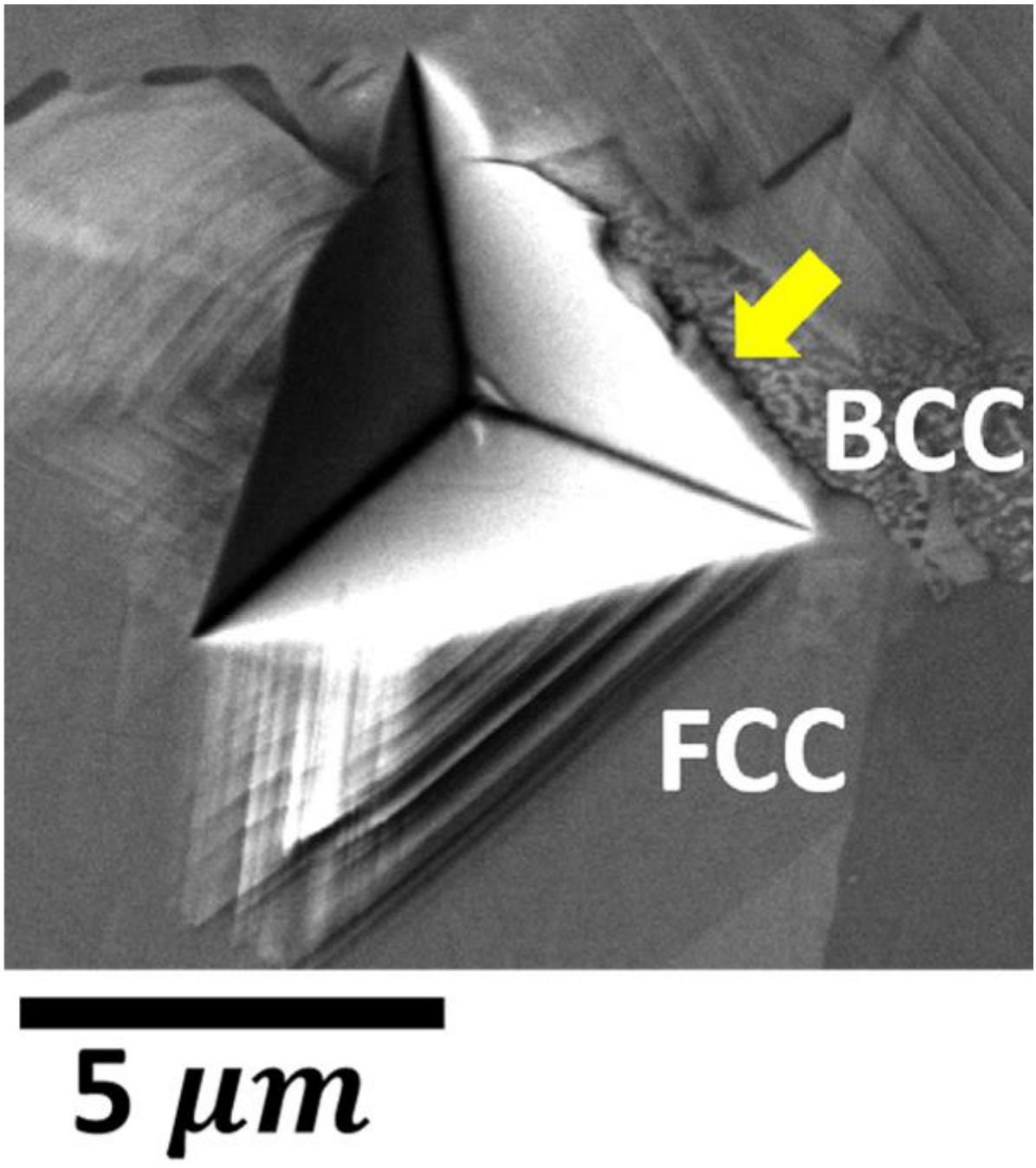

Fig. 11. Experimentally observed fracture initiation along the BCC-FCC interphase boundary for larger indentations (higher imparted total strains).